Particle Morphology of $CuCl_2$ Droplets in Evaporative Spray Drying of Aqueous Slurries by Laser diffraction and Microscopy

M. Slowikowski[1] G. F. Naterer[2], and A. Odukoya[3]

[1] Atomic Energy of Canada Limited , Chalk River, Ontario, Canada, K0J 1J0

[2, 3] Memorial University of Newfoundland, St. John's, Newfoundland, Canada, A1B 3X5

ABSTRACT

New empirical correlations that predict the evaporative spray drying behaviour of slurries are developed in this paper. The analysis examines a single droplet of $CuCl_2$ solution in a continuum drying media. Convection and spray drying modes are reported for the cupric chloride droplet. The results indicate a combination of convection and spray drying modes could improve the drying process. Validation of the experimental results involves comparisons based on non-dimensional analysis. Effects of the Ohnesorge and Nusselt numbers on particle diameter are reported. Analytical models of heat and mass Spalding numbers are developed for the aqueous solution, subject to various drying conditions. Also, the effects of temperature on the atomization flow rate is reported. Particle size diameters are predicted and compared with experimental results using SEM and laser diffraction.

[1] Research Engineer, Atomic Energy of Canada Limited , Chalk River, Ontario, Canada, K0J 1J0
[2] Dean and Professor, Faculty of Engineering and Applied Science, Memorial University, St. John's, Newfoundland, 240 Prince Phillip Drive, St. John's, NL Canada A1B 3X5
[3] Research Project Engineer, Faculty of Engineering and Applied Science, Memorial University, St. John's, Newfoundland, 240 Prince Phillip Drive, St. John's, NL Canada A1B 3X5

Nomenclature

A	Area [m^2]
B	Spalding number, $\left[\frac{\rho_{vs}-\rho_{vb}}{\rho_{vs}}\right]$
Bi	Biot number $\left[\frac{hd}{k}\right]$
Cp	Heat capacity [kJ/kg·K]
d	Diameter [m]
$\bar{d}$	Representative diameter for curve-fitting [m]
$\mathfrak{D}$	Mass diffusion coefficient [m^2/s]
Fo	Fourier number $\left[\frac{\alpha_d t}{r_d^2}\right]$
g	Acceleration due to gravity [m^2/s]
h	External heat transfer coefficient [W/m^2 K]
ΔH_v	Latent heat of vaporization [kJ/kg]
k	Thermal conductivity [W/m K]
L	Length [m]
Le	Lewis number $\left[\frac{\alpha}{d}\right]$
$\dot{m}$	Flow rate [kg/s]
m	Molecular weight [kg/mol]
$\mathfrak{m}$	Molality [mol/kg]
m_i	Measured value [-]
N	Number of parameters [-]
$\aleph$	Drying rate [kg/m^2s]

Nu Nusselt number $\left[\frac{2hD_d}{k_{sol}}\right]$

Oh Ohnesorge number $\left[\frac{\sqrt{We}}{Re}\right]$

p Pressure [Pa]

Pr Prandtl number $\left[\frac{\mu C_p}{k}\right]$

q Parameter of distribution width $[q < 3]$

$\dot{q}$ Heat flux density [W/m^2]

r Radius, radial displacement [m]

R Universal gas constant [KJ / kmol K]

$\mathcal{R}$ Radius of curvature of free surface [m]

Re Reynolds number $\left[\frac{\rho u_{z,0} d_0}{\mu}\right]$

Sh Sherwood number $\left[\frac{2R_d h_m}{\mathfrak{D}_g}\right]$

t Time [s]

T Temperature [^{o}C] or [K]

u x-direction velocity [m/s]

V Volume, molecular volume [m^3]

We Weber number $\left[\frac{\sigma}{{u_{z,0}}^2 \rho r_0}\right]$

X Dry basis moisture content [kg H_2O / kg dry substance]

Subscripts

0 Initial, first

1	Reference temperature, first
2	Desired temperature, second
10	Number mean
20	Surface mean
30	Volume mean
32	Sauter mean
∞	Bulk value
a	air
b	Bulk gas, bulk fluid
c	Critical temperature
cr	Critical
d	Droplet
e	Equilibrium
h	Heat
g	Gas
m	Mass
max	Maximum
mmd	Mass median droplet
mr	Root-mean
s	Surface
w	Water
sw	Wet solid
wb	Wet bulb

wv Water vapor

θ Angle – direction

Superscripts

$*$ Non-dimensionalized

Greek letters

α Contribution to thermal conductivity of ion [-], Thermal diffusivity [m^2/s]

μ Dynamic viscosity [Pa·s]

υ Kinematic viscosity [m^2/s]

ρ Density [kg/m^3]

τ Shear stress [N/m^2]

σ Surface tension [N/m]

σ Parameter describing shape of distribution [-], Bayseian information criterion [-]

ν Stoichiometric coefficient [-]

φ Osmotic coefficient [-]

θ Angle, surface-liquid contact angle [^{o}]

θ Non-dimensional temperature [-]

χ Parameter for chi-squared test [-]

Acronyms

Cu-Cl Copper-Chlorine

DCC	Copper Chloride dihydrate
DPF	Discrete probability function
LALLS	Low angle light scattering, or laser diffraction
ME	Maximum entropy
PCB	Printed circuit board
SEM	Scanning electron microscope
SMR	Steam methane reforming
TC	Thermochemical cycle
TGA	Thermo-gravimetric analysis

1. Introduction

Our way of life, measured by the standard of living and quality of life, is highly dependent on energy and resource consumption [1]**.** Our growing resource consumption has caused CO_2 emissions to grow 188% between 1973 and 2008 [2]**.** About 95% of our transportation energy is based on oil and conventional fuels [3] . As more sustainable methods for transportation are developed, hydrogen has come to the forefront of alternative fuels. Hydrogen is a promising clean energy carrier for the future of the transportation industry.

The Cu-Cl cycle of thermochemical production of hydrogen is a water splitting method for producing hydrogen without the use of fossil fuel. An essential part of this cycle is the drying of products of an electrolysis reaction. The complete cycle for this process is shown in Fig. 1. This paper investigates the copper chloride dihydrate (DCC) electrolyte drying process within the Cu-Cl cycle. Aqueous cupric chloride, a product of the electrolysis

reaction, is required as dry solid particles for the subsequent hydrolysis reaction in the Cu-Cl cycle.

There are various configurations of the Cu-Cl cycle for hydrogen production. The configurations have corresponding advantages and drawbacks as outlined by Orhan [4][4]. The processing of aqueous DCC solution is an essential step in the five and four step variations of the cycle. This paper focuses on the four step cycle (Table 1). Aqueous DCC is a product of the electrolysis reaction, and is required in the form of dry solid particles for the subsequent hydrolysis reaction in a fluidized bed. For this cycle, fast and efficient recovery of aqueous DCC is essential. Some possible methods for recovering DCC from the electrolyte are shown in Fig. 2.

The most efficient conversion mechanism is determined by taking measurements of various parameters using different processing methods, as well as collecting physical data related to the drying of DCC. The feed and product characteristics should also be determined. These parameters, and the characteristics of different processing methods, will affect which recovery process is ultimately chosen. Spray drying is a viable option for the Cu-Cl cycle as it can be easily integrated with the fluidized bed, and the properties can be easily controlled.

Jangam and Thorat [5] dried ginger in a lab-scale spray dryer at temperatures from 120-160^{o}C to determine product characterization for commercial use. A similar spraying technique is discussed in this paper. Other studies specifically aimed at spray drying DCC in the Cu-Cl cycle have been presented. Daggupati et al. [6] studied the effects of atomization conditions and flow rates on particle formation during cupric chloride, sodium bicarbonate, and sodium carbonate drying in a lab-scale spray dryer. However, to our knowledge, there has been no comprehensive study to determine particle size morphology for DCC product

use in the fluidized bed of the Cu-Cl cycle. This paper aims provide a methodology to characterize the droplet with the aim of advancing the knowledge on how the spray drying process could be optimized for a desired operating condition.

The morphology of spray dried particles was found to depend significantly on the dried material. Daggupati et al. [7] dried DCC and found at temperatures higher than 120^{o}C, the spray dried particles formed hollow spheres. However, at lower temperatures, some sharp-edged amorphous particles were formed. Below 80^{o}C, all particles were sharp-edged and amorphous. The laser diffractometer can be used to reduce the effect of porosity and agglomeration of DCC particles on the measured diameter of the particle. The distribution of particles using the measurements from other dried substances can be compared.

Effective control of particle size is the most desired goal in spray drying. Often one particle size and droplet size are taken to represent the whole set. Various definitions of diameters are used in industry, as shown in Table 2. Various distributions are used to help with industrial processes for which particles are used in different processes, whereby volume, surface area, or the number of particles will have greater importance. For spray drying, the Sauter mean diameter is most often used.

Studies have been conducted to determine how particle size is affected by various parameters. Correlations are often used to describe these parametric influences on droplet or particle size. Stahl et al. [8][10] found that the particle size increases with decreasing nozzle flow. Birchal et al. [9] found a slight counter-current trend; however this was due to a rotary nozzle used in their experiments. Thybo et al. [10] also derived a correlation for spray dried particle size using results from a lab-scale study. The conditions under which the correlation

was completed and materials dried should be noted, since different materials can exhibit different drying characteristics under the same conditions.

Babinsky and Sojka [11] conducted a comprehensive particle size distribution survey and found two ways (classical and analytical) were most often used to determine particle size distributions. Recently, analytical approaches have been developed to predict the particle size distribution. Two methods, namely the maximum entropy method (ME), and the discrete probability function (DPF) method, both are non-deterministic methods used to predict the final particle distribution based on different underlying assumptions. This paper uses the physical characteristics and changes between experiments, rather than a non-deterministic method for extrapolation of data. Liu et al. [12] used Edwards and Marx theory to show that fluid properties affect the atomization in spray dryer. The results indicate the internal design of atomizer can distort multiphase flow in the atomizer, which results in unsteadiness in the atomizer. Other studies have investigated the effect of Nusselt number, viscosity and concentration on the atomization in the spray dryer [13-15].

Walton and Mumford [16] conducted a comprehensive study of particle morphology and found that particle size, size distribution, particle shape (irregular vs. spherical shape), moisture content, and the hygroscopy of the powder all contributed to the flowability of the powder. Thybo et al. [10] dried acetaminophen and polvinylpyrrolidone K-30. At higher temperatures, the particle surface was much smoother, because many smaller crystals are formed.

Meenan et al. [17] found that spray dried burkite droplets had a high overall porosity due to crystals aggregating edge to face, and edge to edge. The effective wall thickness of

large and small particles didn't change. However, the bulk crystal in smaller particles was denser. Larger particles were also found to have a higher tendency to be hollow.Ambike et al. [18] determined that additives can be used as a means of decreasing the crystallization of particles. Additives in spray drying DCC could be detrimental to the Cu-Cl cycle. These additives would build up due to a continuous need in spray drying and thus decrease the cycle efficiency.

Many previous experiments have been conducted to determine properties from convective drying of DCC. Mohamed and Halawy [19] completed non-isothermal TGA measurements on copper (II) chloride dihydrate efflorescence**.** Polyachenok et al. [20,21] used tensimetric methods to measure the equilibrium water vapor pressure for the dehydration of solid cupric chloride dehydrate. Polyachenok [21] noted that technical issues with current experimental methods for thermodynamic quantities existed. Busscher et al. [22] studied the influences of additives on the evaporation and subsequent dewetting and crystallization of various concentrations of cupric chloride solution. Keskitalo et al. [23] studied the removal of copper from spent DCC solutions in the PCB industry. Most of the applications involve other chemical reactions, without reusing the final products in the cycle as done in the Cu-Cl cycle. To our knowledge, there are no studies on the drying rate of cupric chloride in slurry form, and no comparisons made with past literature. This paper determines the drying rate based on experimental measurements.

Although extensive research has been conducted on copper (II) chloride, most of the past research was not applied to the Cu-Cl cycle. Further research is required to understand its properties at various levels of processing within the cycle. Various aspects of drying, such

as determining particle size and distribution, are investigated in this paper. DCC solution drying, spray drying, and convective drying are also examined.

2. System description

Spray drying is examined to determine its physical viability for DCC processing. Convective drying is also studied and modelled to determine drying rates at various temperatures. This information will be useful in predictive modelling of the drying process. For a fluidized bed to be effective in the copper-chlorine cycle, DCC particles should have controlled properties to allow the fluidized bed to operate quickly, reliably, and efficiently.

From the two volatile compounds, excess hydrochloric acid in the feed will inhibit the reaction, and excess water will assist the reaction. However, by the time when the reactants (products from spray drying) are raised to 300-400^{o}C, all volatile compounds will evaporate. This suggests that the final spray drying products need not be completely dry before going into the fluidized bed. In this paper, drying occurs by vaporization of volatile substances by supplying heat to wet feedstock, yielding a dry solid product. Water is the volatile substance. A liquid solution or slurry with dissolved solids is heated. Moisture vaporizes from the liquid, leaving a solid product. Moisture is divided into two groups: bound moisture and (moisture at vapour pressure higher than the pure liquid) and unbound moisture (moisture in excess of the bound moisture; exerts a vapour pressure equal to the pure volatile).

In a spray drying apparatus, shown in Fig. 3, liquid solution is pumped with a peristaltic pump to the pneumatic atomization nozzle. Compressed air is mixed with the liquid solution in a two-fluid nozzle. Drying air is drawn from the atmosphere through a filter compressor

through a flow valve to the electric heater. The dried powder product is separated from the air using a cyclone separator. Before releasing the air, a venturi scrubber is used to clean the air free of any suspended particulate.

When a droplet is formed, drying and evaporation continue in stages. First, the droplet is heated to the wet bulb temperature of the surrounding gas. The evaporation and boiling processes commence. As more volatiles evaporate from the droplet, saturation conditions develop on the droplet surface. Local nucleation of salt crystals begins and a crust is formed as these crystals grow toward each other. As the crust is formed, water is brought to the surface through pores which are formed in the crust. This is the onset of the falling rate drying period. After all water leaves the droplet as it becomes a solid particle, the particle is heated to the equilibrium temperature with its surroundings.

3. Initial droplet heating

3.1 Problem formulation

The initial heating starts when the fluid exits the nozzle flow. This heating period occurs on the order of tenths of a second [24]. For a spherical droplet with isotropic properties, an energy balance at the initial stages of droplet heating in spherical coordinates [25]] is reduced using the Laplacian representation of the temperature. The material derivative of T_d in spherical coordinates is defined as:

$$\frac{DT_d}{Dt} = \frac{\partial T_d}{\partial t} + u_r \frac{\partial T_d}{\partial r} + \frac{u_\theta}{r}\frac{\partial T_d}{\partial \theta} + \frac{u_\varphi}{rsin(\theta)}\frac{\partial T_d}{\partial \varphi} \quad (1)$$

As previously noted in past studies [24-27], a lumped capacitance heat and mass transfer model can be assumed if the spatial temperature distribution within the droplet is sufficiently

small. The lumped capacitance model implies that heat conduction within the droplet is much faster than heat convection away from the droplet surface. It models the heat transfer process from the droplet to its surroundings in one lumped process. To use the lumped capacitance model, the Biot number must be below 0.1.

The Fourier number is $Fo = \alpha_d t / r_d^2 > 0.1$ and the temperature dependence with time must be considered. Internal convection was determined negligible based on a Biot number analysis, due to the small droplet diameters. A Biot number of 0.5 was calculated based on the limits of the experiments. Internal convection is negligible if the Biot number is much less than 0.1. In the centre of the droplet, there is only a time dependence on temperature. At the outside of the droplet, the temperature is influenced by the surrounding gas temperature and thermal conductivity of the droplet. For surface drying to start, the droplet temperature is brought above the wet bulb temperature for the current air moisture content.

3.2 Evaporation and shrinkage processes

After the initial heating process, the droplet continues to dry in a constant drying period. Evaporation and shrinkage occur from the droplet surface. The following analysis uses reduced forms of the transport equations similar to the assumptions of Yang's model [28]. In evaporation analysis, the equivalence of heat and mass transfer can be used [25,29]. This is justified when the Lewis number is on the order of unity. For droplets, the Nusselt number for heat transfer and the Sherwood number for mass transfer are compared. Despite the prevalence of the Ranz and Marshal [30]equation for the Nusselt number in literature, Hoffman and Ross [31] proposed a more accurate solution for the Nusselt number for $1 < Re \leq 400$ [32]:

$$Nu = 1 + (1 + RePr)^{1/3} Re^{0.077} \quad (2)$$

This equation fits experimental data for non-evaporating drops by ±3%. To determine the effects of evaporation, two hydrodynamic methods are considered. At the surface of an evaporating droplet moving in a surrounding fluid, the following equation describes the mass diffusion and convective mass flow (Stefan flow) [33]:

$$\frac{\dot{m}_d}{4\pi R^2} = \mathfrak{D}_v \frac{d\rho_v}{dR} - \mathfrak{D}_g \frac{\rho_v}{\rho_g} \frac{d\rho_g}{dR} \quad (3)$$

The left side term is the mass flux from the droplet. The middle term refers to diffusion effects and the third term represents the Stefan effects. Assuming that the vapor diffusion coefficient is the same as the total gas diffusion, $\mathfrak{D}_g = \mathfrak{D}_v$, and the total density of the gas is constant ($v_v \rho_v + v_g \rho_g = \rho_{total} = const$). Integrating from $R = R_{d \to \infty}$:

$$\dot{m}_d = 4\pi R^2 \mathfrak{D}_v \rho_{total} \ln(1 + B_M) \quad (4)$$

where B_M is the mass transfer Spalding number:

$$B_M = \frac{\rho_{vs} - \rho_{vb}}{\rho_{vs}} \quad (5)$$

Following the definition of the Sherwood number $\left(Sh = \frac{2R_d h_m}{\mathfrak{D}_g}\right)$ and heat transfer coefficient, h_m is defined whereby:

$$\dot{m}_d = 4\pi {R_d}^2 h_m (\rho_{vs} - \rho_{vb}) \quad (6)$$

Eq. (2) can be re-written:

$$\dot{m}_d = 2\pi R_d \mathfrak{D}_g \rho_{total} Sh^* B_M \quad (7)$$

The Sherwood number is:

$$Sh^* = \frac{\ln(1+B_M)}{B_M} Sh_0 \tag{8}$$

where Sh_0 is the Sherwood number in the absence of evaporation. Performing an energy balance at the surface of the droplet, the following equation is obtained:

$$4\pi {R_d}^2 k_g \frac{dT}{dR} = -\dot{m}_d c_{pv}(T - T_s) - \dot{m}_d \Delta H_v(T_s) + |\dot{q}_d| \tag{9}$$

where the left side is the heat supplied from the surroundings. The first right term is the heat required to initially heat the droplet, the second term describes the vaporization, and the final term is the heating of the droplet's vapor to ambient conditions. Integrating Eq. (9) over $R = R_{d\to\infty}$ and $= T_{s\to g}$, the mass flow rate of the droplet can be written as:

$$\dot{m}_d = -\frac{4\pi R_d k_g}{c_{pv}} \ln(1 + B_T) \tag{10}$$

where B_T is the heat transfer Spalding number. Following the definition of the Nusselt number $\left(Nu = \frac{2hd}{k_{sol}}\right)$ and Eq. (6) for the heat transfer coefficient, Eq. (10) can be rewritten as:

$$\dot{m}_d = 2\pi R_d \frac{k_g}{c_{pv}} Nu^* B_T \tag{11}$$

The Nusselt number here is:

$$Nu^* = \frac{\ln(1+B_T)}{B_T} Nu_0 \tag{12}$$

Also Nu_0 is the Nusselt number in the absence of evaporation, defined by $Nu = 2 + Re^{1/2}Pr^{1/3}$. Eq. (7) and (11) have very similar forms. They differ by their definitions of the Spalding number:

$$B_T = (1 + B_M)^{\alpha} - 1 \tag{13}$$

$$\alpha = \frac{c_{pv}}{c_{pg}} \frac{1}{Le} \tag{14}$$

The Reynolds number determines the ratio of shear forces to momentum forces, while the Weber number relates surface tension forces to momentum forces. A correlation describing the initial jet atomization phenomenon and droplet size from initial parameters has the form:

$$\frac{d_{32}}{d_0} = C \cdot We^{\alpha} \cdot Re^{\beta} \tag{15}$$

Often in sprays, the Ohnesorge number is introduced, which is a ratio of the Weber and Reynolds numbers:

$$Oh = \frac{\mu}{\sqrt{\rho \sigma L}} = \frac{\sqrt{We}}{Re} \tag{16}$$

Since all three numbers (We, Oh, and Re) are not independent of each other, a droplet size correlation must include only two out of three numbers. Eq. (15) is adapted to use the Ohnesorge number. It has the following form:

$$\frac{d_{32}}{d_0} = C \cdot We^{\alpha} \cdot Oh^{\beta} \tag{17}$$

Eq.(17) is a useful estimate of initial droplet size. However, since only one fluid equation is used, the relative differences between the gas for atomization and the liquid are not

considered. The Buckingham-pi theorem is used to determine C, $\alpha, and\ \beta$. The Reynolds number was estimated as:

$$Re = \frac{\rho u_{z,0} d_0}{\mu} \tag{18}$$

Further details of the mixture viscosity, density, velocity and droplet diameter were reported by Slowikowski [34].

3.3 Empirical correlation

A distribution analysis is used to compare physical changes between experiments. The particle size equations are deterministic to describe the range and type of data observed. All particle distribution functions are fitted to the data, to determine the type of distribution of the experiments and the spread of the distributions.

All particle distribution functions follow certain characteristics. The total number of droplets below a minimum diameter and above a maximum diameter should be small. By using a maximum diameter, the effects of agglomeration can be neglected. A diameter that does not distort the shape of the distribution function must be used to ensure validity of the model. The maximum diameter for the data collected during the experiment is $175\mu m$.

$$\lim_{d \to 0} \int_0^d f(d)\mathrm{d}d = 0 \tag{19}$$

$$\lim_{d \to \infty} \int_d^\infty f(d)\mathrm{d}d = 0 \tag{20}$$

The distributions are positive and normalized. Distribution models are chosen to be fitted to the measured size distributions. The distributions are chosen based on previously applied results for spray drying, as noted by Babinsky and Sojka [11].

The first distribution to be fitted is the Log normal distribution:

$$f_1(d) = \frac{1}{d(ln\sigma)\sqrt{2\pi}} exp\left\{-\frac{1}{2}\left[\frac{ln(d/\bar{d})}{ln\sigma}\right]^2\right\} \quad (21)$$

where d is the predicted particle size, σ is a parameter describing the shape of the distributionn($\sigma > 0$), and $\bar{d}$ is a representative diameter for curve fitting.

The probability of obtaining large particles becomes infinitesimally small at the trailing end of a Log-normal distribution, allowing an upper limit to be set on the probability. Above this upper limit, the probability of obtaining particles is zero. The probability distribution function is defined as follows:

$$f_2(d) = \frac{\delta d_{\max}}{\sqrt{\pi} d(d_{\max}-d)} \exp\left\{-\delta^2\left[\ln\left(\frac{ad}{d_{\max}-d}\right)\right]^2\right\} \quad (22)$$

where $= \frac{d_{\max}}{\bar{d}}$, $\delta = \frac{1}{\sqrt{2}(\ln\sigma)}$, σ is the width of the distribution $(\sigma > 0)$, $\bar{d}$ is the logarithmic mean size of the distribution, and $d_{\max}$ is the maximum permissible droplet diameter.

The root normal distribution, originally defined by Marshall and Tate [35], was applied to volume distributions in sprays. The probability distribution function is given as follows:

$$f_3(d) = \frac{1}{2\sigma\sqrt{2\pi d}} \exp\left\{-\frac{1}{2}\left[\frac{\sqrt{d}-\sqrt{\bar{d}}}{\sigma}\right]^2\right\} \quad (23)$$

The Rosin-Rammler distribution [36] originally found its application in coal particle distributions. The probability distribution function is defined in the following way:

$$f_4(d) = q\bar{d}^{-q} d^{q-1} \exp\left\{-\left(d/\bar{d}\right)^q\right\} \quad (24)$$

where $q \geq 3$ is a value representing the width of the distribution, with large values of q giving narrow sprays. However, for physically meaningful spray distributions, $q > 3$, as smaller values of q will yield negative values for distributions.

To determine the best fit for the collected data, two different tests were performed. Initially, the Chi-squared test was used:

$$\chi^2 = \sum_{i=1}^{N} \frac{(m_i - p_i)^2}{p_i} \tag{25}$$

where χ , is the value to be minimized, N is the number of values, m_i is the true measured value, and p_i is the predicted value based on the curve to be fitted. It was observed that the Chi-squared test gave skewed results due to small sample sizes in the analysis. Therefore, the Bayesian criterion was chosen as a tool for curve-fitting. The Bayesian information criterion is denoted as follows:

$$\sigma^2 = \frac{1}{N-1} \sum_{i=1}^{N} (m_i - p_i)^2 \tag{26}$$

3.4 Convective drying

Convective drying in a conventional oven was used to determine the drying rate, $\aleph_W$. The drying rate is determined by a first order linear equation proportional to the free moisture content [37]:

$$\aleph_W = -\frac{1}{A_S} \frac{dm_{SW}}{d\tau} = \frac{dm_{SW}}{A_S} \frac{d\bar{X}}{d\tau} \tag{27}$$

where $\bar{X} = X - X_e$, and X_e is the moisture content of the dry solids at equilibrium with their surroundings. For DCC, above 100°C there is no chemically bound moisture and $X_e = 0$.

The moisture content, X, is $X = \frac{m_{SW} - m_S}{m_S}$ and $m_{SW} = m_W + m_S$. The wet mass, mass of moisture, and dry mass are m_{SW}, m_W , and m_S, respectively. Also, A_S is the surface area in contact with the drying surface. The characteristic rate drying curve (CDRC) model is attractive for use as a convective drying model since a version modified for particles is used in spray drying. By expanding the differential terms in Eq. (27), the following equation is obtained:

$$\aleph_W = (X - X_e)[C(T_b - T_{wb})]\frac{m_S X}{A_S} \tag{28}$$

where, T_b is the bulk temperature, which is controlled, T_{wb} is the wet bulb temperature, m_S is the mass of the solid, and A_S is the surface drying area. While C is a constant determined when equating both sides of Eq. (28) after experimentation. The drying rate is used to obtain the mass of evaporated moisture during the drying process. Substituting for $\dot{m}_d$ in Eq. (11), the value of B_T can be calculated. B_T is valid for both convection and spray drying. The method of estimating the moisture content will vary for spray drying as compared to convection drying.

4. Experimental setup and procedures

In the experiments, the hot air inlet temperature, solids concentration, flow rates, atomization pressure, nozzle diameter, and liquid initial temperature were all varied. Each parameter was varied separately to determine its effect on the output parameters in isolation. The ambient air humidity and temperature were noted for each experiment using a digital barometer. For some experiments, the ambient air temperature varied significantly.

Experiments on different days were conducted to determine the effect that ambient air humidity (22-38%) would have on the dependent variables.

Experiments were conducted with a Yamato model D-41 spray dryer. A schematic diagram of the experimental setup for low-grade heat utilization is shown in Fig. 3. The dryer was modified slightly from its manufactured state to avoid irreversible corrosion caused by spray drying of corrosive cupric chloride solution. Two separate gas orifice sizes were used in the titanium nozzles: 0.7mm and 1.5 mm diameters. Stainless steel parts downstream of the nozzle were coated with a thin layer of Viton. All glass parts of the drying chamber, cyclone separator, and product vessel were kept in an uncoated state. Also, a venturi scrubber was used to clean the flue gases of cupric chloride particles, which were not captured inside the cyclone.

The particle morphology was investigated with a JEOL JSM-6400 scanning electron microscope (SEM). Black carbon tape was applied to the SEM aluminum stub, and the powder sample was stuck to the carbon tape. The crystal structure observed under the SEM was anhydrous copper (II) chloride. Laser diffraction was used to determine the particle size and distribution, using a Microtrac S3500 unit.

The drying air entered the dryer at the top and was then heated. It entered the drying chamber, and left through the cyclone separator and finally the scrubber. A peristaltic pump was used to transport the atomization liquid to the two-fluid nozzle. A flow meter was installed to measure the atomized air flow rate. To measure the atomization liquid flow rate, the initial and final time of experimentation and volume of liquid were recorded. K-type thermocouples were installed to measure the exiting air humidity and temperature.

Analytical grade (98%) copper chloride and commercial grade de-ionized water were used in all experiments. All copper chloride was first dried in a conventional oven at 110^{o}C and used in the anhydrous form during experiments, to eliminate error in hydration levels. Air was taken from the surrounding room at ambient temperature and humidity. It was filtered inside the spray dryer, and heated.

The atomization air and drying air flow rate were measured with a separate air flow meter. The flow pressures were measured with a pre-installed pressure gauge. The drying air inlet and outlet temperatures were measured with K-type thermocouples. The atomization liquid flow rate was varied and measured based on the time required for the experiment to complete and the volume of liquid.

Through SEM microscopy, the surface area of particles can be determined based on the observed area in the micrograph. There is a large uncertainty ($\pm$20%) in underrepresenting the particle population using SEM microscopy. LALLS (low angle light scattering, or laser diffraction) was used to determine the particle size, as verified with SEM microscopy. SEM microscopy was also used to determine the particle morphology. The droplet size is determined using the final Sauter diameter measure from the SEM image.

The two bars on either side of the trend line in Fig. 4 represent 95% confidence intervals. If a correlation estimates the final diameter within ±40% of the data, the correlation is made as accurate as the data. If non-spherical particles (equivalent diameters are much less accurate) are not included, the intervals fall to ±20%, as shown in Fig. 5.

The unit's particle range is 0.024-2800μm. Each sample was taken a minimum of three times for repeatability. The machine was allowed to operate once without any new product introduced between samples to minimize error. The analyzer gives the particle number mean

diameter, area mean diameter, volume mean diameter, and particle size distribution. The Sauter mean diameter was used to calculate the span. The span of the powder is calculated in the following way:

$$Span = \frac{(d_{90\%} - d_{10\%})}{d_{50\%}} \quad (24)$$

where 10%, 50%, and 90% are the diameter values at the 10^{th}, 50^{th}, and 90^{th} percentiles, respectively. The distribution of the data was also obtained from the Microtrac readouts. This data is used to determine the distribution model that best fits the data. The distributions were compared based on the Chi-squared test and Bayesian information criteria.

The moisture content of the samples was analyzed with a conventional oven. A collection of samples were prepared with 4-5g of dried copper (II) chloride powder, and the mass was recorded. A sample was kept at 105^{o}C and removed from the oven every 10 minutes, and placed into a desiccator for one minute. another mass of the sample was taken, and the sample was returned to the oven. The dry mass was taken when the difference between successive measurements was stabilized. The measurements appeared to stabilize after six readings. The largest variation in the data occurred after complete drying occured at 130^{o}C. The instrumentation accuracy is determined to be within ±0.005g.

The ambient air humidity and temperature were noted for each experiment using a digital barometer. Two experiments with different extraction time intervals were conducted for selected temperatures to determine the effect of heat loss to the environment while the door was left open for approximately one second to remove the sample bottle.

Sample bottles were weighed for the initial empty mass, mass with 4.5g ±0.5g of sample, and after the prescribed time of drying (allowing cooling in a desecrator for 1

minute). The sample bottles were all returned to the dryer after experiments, to determine the bone dry mass of the DCC sample, and the initial moisture content.

A conventional oven is used to perform the experiments for convection drying. A similar sample bottle used for the spray drying experiment is inserted in the oven. The temperature was controlled at different set points, while the air flow rate was kept constant. A mechanical scale with four digit accuracy was used for all mass measurements. Sample bottles were cleaned with de-ionized water and acetone between experiments. Their masses were measured before each experiment, with their lid placed beside the bottle on the scale. Samples of 4.5g were then taken, and the bottles had their lids placed on while other samples were prepared. All samples were placed inside the oven at the same time, with their lids removed. Upon removing samples from the oven, their lids were replaced, and the bottles were placed into a desiccator to allow sample bottles to cool for one minute before placing them on the scale.

5. Results and discussion

Correlations are compared with experimental results in this section. In Fig. 6, a non-dimensional comparison of the droplet diameter dependence on the Ohnesorge and Nusselt numbers is reported. There is a strong dependence on the Ohnesorge number, while the dependence on the Nusselt number is less pronounced.

In the process of spray drying of aqueous cupric chloride, the volatile compounds (water and some hydrochloric acid) evaporate from the droplets generated by the atomization nozzle. Because the volatile compounds evaporate at the surface of the droplet, nucleation and precipitation occur on the surface. This causes crystals to form, and grow internally into the droplet. The internal crystal structure of the particles is fine. Many small crystals are

formed. In Fig. 7, there is an organized concentric pattern formed in the internal crystal of the particle, and the pattern is much coarser. The inner concentric pattern appears darker with a higher concentration of particles.

Comparing the SEM images in Fig. 7 and 8, higher temperatures increase the number of nucleation points. Due to the increased number of crystals as evident in Fig. 8, there is less precipitate per crystal, and the crystals are much smaller in size. This difference in crystal formation is further evident with the difference in color between the 200^{o}C and 120^{o}C particles. In the images on the left of Figs. 7 and 8, the SEM image of the lower temperature shows a darker concentration of crystals at the center, which is not evident at 200^{o}C

At different temperatures and operating conditions, different drying mechanisms were dominant. This was clearly visible due to a color change of the collected samples from higher to lower temperatures. When completely dry, the anhydrous $CuCl_2$ forms crystals of a maroon-brown color, while the completely hydrated powder is turquoise-blue. When there is a mixture of crystals, the color ranges include light green, to an almost orange color, then to brown. The 60^{o}C experiments yielded blue-green particles. The 120^{o}C experiments yielded yellow-green particles, while the 200^{o}C experiments yielded brown / yellow-brown particles.

As the drying rate slows, the number of nucleation points drops, and particles form more distinct patterns as observed in Fig. 9. For the purpose of this analysis, the wall thickness was assumed uniform at all points in the particle wall. Measurements were taken for the wall thickness, as shown in Fig. 10. Particle size analysis was done using ImageJ, an image processing software package. SEM images were used as input to the software, and calibration was done with the distance reference given with the SEM image. As these images

have a maximum pixel resolution, the uncertainty in the image analysis was closely related to the uncertainties in the pixel resolution. Each image had its separate calibration, and therefore the uncertainty in each image was different due to slightly different scales. The uncertainty was estimated based on the data collected, the precision error, and the bias error of the equipment. The calculated uncertainty was 15% of the measured data.

The largest span was observed with the highest temperatures. It is expected that the higher temperatures generate smaller particles, due to the differences in densities between the hydrous and anhydrous forms, and due to faster drying times, meaning less time to agglomerate during the drying period. At higher temperatures, tighter lattices with smaller crystals were formed, corresponding to faster drying times. The reason for this large span was attributed to the storage of dried particles. Although the particles were stored in sealed containers, they were slowly subject to atmospheric conditions. This re-hydration, along with agglomeration, was removed from further analysis of the final particle diameter.

For an inlet temperature of 200^{o}C, round particles with a narrow particle size distribution are expected as shown in Fig. 8. The laser diffractometer reading in Fig. 11, is based on the SEM Image in Fig. 8. The experimental data for the laser diffractometer readings is shown in Table [3], which is used to explain the particle size distribution. From the results of the laser diffractometer in Fig. 11, it is evident that the particle size distribution is bimodal. About 37.7% of the volume of the particles has an average size of 229.5um. This is a relatively large particle size. From the percentile data, the span is calculated for each sample. These results are verified with the SEM images shown in Fig.8. Due to the low pressures in the scanning electron microscopes, the particles viewed under the SEM are completely dry. Since the particles were not completely dry upon leaving the spray dryer

under most runs, it should be expected that the particles observed under the laser diffractometer would be slightly larger than under the SEM.

This volume change is in proportion to the changes in crystal structure of cupric chloride as it changes from dihydrate to anhydrous form, as with its density. The anhydrous form has a density of 3.386 /cm^3 while for the dihydrate, it is 2.51 g/cm^3. Therefore, the difference in volume taken up by the hydrate to the anhydrous form is about 34.5%. Assuming round solid particles, this corresponds to a difference in diameters of 10.5%, assuming that the final product is fully hydrated. This was most evident during the low temperature experiments.

From one of the samples observed (Fig. 12), the final moisture content was 0.928%, corresponding to a diameter-difference of 0.0974% compared to the theoretical particle diameter $\left(\mathrm{D}_{32,\mathrm{final}} = \frac{3}{4\pi}(\mathrm{V}_0)^{1/3}\right)$, below the experimental uncertainty. The Sauter diameter from the SEM is much smaller than 229.5μm, as recorded by the laser diffractometer. A method for excluding the agglomeration effects from laser diffraction was devised to determine the true particle diameter. Using the peak data from the laser diffraction data, the following equation was determined, correlating the peak data to the Sauter diameter:

$$\sum_{i=1}^{N\ peaks} \frac{\overline{m_i}\cdot(Vol\%)}{100} = D_{32,calculated} \cong D_{32,measured} \tag{29}$$

Using the peak summation equation and the observed histogram for the laser diffractometer, the agglomeration was excluded:

$$D_{32,no\ aglom.} = \sum_{i=1}^{N-largest} \frac{\overline{m_i}\cdot(Vol\%)}{100-(Vol\%)_{largest}} \tag{30}$$

In this way, all three samples were included in determining a representative Sauter diameter for each experiment, while the effects of agglomeration were excluded.

Equivalent droplet diameters for each particle were determined using the process in Fig. 13.The central void fraction can be obtained by comparing the wall thickness to the particle diameter. The wall void fraction could be estimated by making a model for dentricle packing. Some final particles were not hollow or spherical (as with the lower heat transfer cases). The void fractions are not applicable and not considered. By recording the final moisture content and determining the air void packing, the equivalent droplet size was obtained from the spraying phenomenon.

Various distribution models were compared to determine the best fit to the spray dried particle distributions. Log-normal, upper-limit log, root-normal, and Rosin-Rammler distributions were all compared against the data sets. Various cases were chosen to conduct the analysis. Fig. 14 shows the best-fit curves for the 2nd run at 80^{o}C. The Log-normal distribution provides the best fit for the data. The experimental case in Fig. 8 is used to explain the results in this paper. The air inlet air temperature was 80^{o}C, and air outlet temperature was 40^{o}C. The drying air flow rate was 0.8m^{3}/min. The atomization liquid flow rate was 0.58litres/hour, while the atomization pressure was 4bar, and the solids concentration was 9%.

Fig. 15 shows the SEM graphs of these particles. The particle shape was found to be closely agglomerated, and mostly non-spherical. The final moisture content was 27%. The lowest Bayesian value is the most desirable. Table 4 shows the final resulting parameters for all distribution models. There is a clear trend for the average particle size $(\bar{d})$ to decrease

with increasing temperature. The particle size distribution, as determined by the value of sigma, also decreases with increasing temperature. It was seen that agglomeration had a significant role in determining the size of particles. Agglomeration causes the sizes of particles to appear larger than via laser diffraction. This phenomenon is visible in the SEM images.

These experiments were used to calculate the drying rate under various temperatures, for application in the characteristic rate drying curve. The drying rate equation can be directly applied to a CFD code for spray drying predictions. The results from the convective drying experiments are shown in Fig. 16. A linear fit is shown for each drying rate. The initial moisture content of the slurry for the convection experiment was determined by conventional means of completely drying the sample, determining the bone dry mass, and calculating the initial moisture content through the initial mass. Due to the nature of the slurry, there was a large variation (21-27%) with the room air temperature between 21°C and 29°C and with the initial moisture content. Therefore, a method was devised to determine the drying constant of the DCC slurry at the given temperature. The initial three values were omitted in determining the drying constant. These values have a higher drying rate than the average value due to the surface effects of drying.

The average slope of the remaining cases was determined afterwards. The data points were then fitted to the new line, to determine how well the data fit, through an r-squared value, as shown in Fig. 17. The uncertainty of the measured data was estimated to be about ±10%. The measured convection drying rate falls below the drying rate of the dihydrate (a slope of -0.001959 $gm^{-2}s^{-1}$ for the slurry, and a slope of -0.001228 $gm^{-2}s^{-1}$ for the dihydrate at 105°C). This was expected, since the water molecules are bonded to the crystal lattice in

the dihydrate. These values were used to calculate the drying rate of the water over the copper (II) chloride, N_v, to be used to determine the value of B_T, the constant in Eq. (10). The equation is re-arranged to solve for B_T for the experiments conducted. The variability in B_T is ±20%. There is a slight temperature dependence on B_T. The convection drying rates have the same order of magnitude in other applications, such as those observed by Lin and Chen [38].

5. Conclusions

As part of improving the Cu-Cl cycle, DCC electrolyte processing has been conducted to determine energy requirements, drying rates under various operating conditions, and property control for adaptation into the cycle. A new correlation based on input parameters was developed for determining the particle size. The results were used to estimate various parameters. This correlation developed for estimating the particle diameter based on the Ohnesorge and Weber numbers can assist in predicting fluidization for the downstream process of the fluidized bed, and increase the energy efficiency of the Cu-Cl cycle. The Log-normal distribution performed well for the temperature range. The most accurate distribution for spherical particles was the Rosin-Rammler distribution. The distribution fitting process will assist in determining narrow distributions, which allow for better fluidization. This information will be useful in CFD modeling of DCC drying, and future scale-up of the Cu-Cl cycle.

Acknowledgements

Financial support from Atomic Energy of Canada Limited and the Ontario Research Excellence Fund is gratefully acknowledged. The support of the members of the Clean Energy

Research Laboratory (CERL) of University of Ontario Institute of Technology, Oshawa, ON, is also acknowledged.

Reference List

[1] W.P. Nel, C.J. Cooper, Implications of fossil fuel constraints on economic growth and global warming, Energy Policy. 37 (2009) 166-180.

[2]] International Energy Agency, Key World Energy Statistics 2007, OECD/IEA, Paris, France, 2007.

[3] S.C. Davis, S.W. Diegel, Transportation Energy Data Book. Edition 22, Diane Publishing, Oakridge, Tennessee, 2002.

[4] M.F. Orhan, I. Dincer, M.A. Rosen, Design of systems for hydrogen production based on the Cu-Cl thermochemical water decomposition cycle: Configurations and performance, Int. J. Hydrogen Energy. 36 (2011) 11309-11320.

[5] S.V. Jangam, B.N. Thorat, Optimization of spray drying of ginger extract, Drying Technol. 28 (2010) 1426-1434.

[6] V.N. Daggupati, G.F. Naterer, K.S. Gabriel, Diffusion of gaseous products through a particle surface layer in a fluidized bed reactor, Int. J. Heat Mass Transfer. 53 (2010) 2449-2458.

[7] V.N. Daggupati, G.F. Naterer, K.S. Gabriel, R.J. Gravelsins, Z.L. Wang, Effects of atomization conditions and flow rates on spray drying for cupric chloride particle formation, Int. J. Hydrogen Energy. 36 (2011) 11353-11359.

[8] K. Ståhl, M. Claesson, P. Lilliehorn, H. Lindén, K. Bäckström, The effect of process variables on the degradation and physical properties of spray dried insulin intended for inhalation, Int. J. Pharm. 233 (2002) 227-237.

[9] V.S. Birchal, M.L. Passos, G.R.S. Wildhagen, A.S. Mujumdar, Effect of spray-dryer operating variables on the whole milk powder quality, Drying Technol. 23 (2005) 611-636.

[10] P. Thybo, L. Hovgaard, J.S. Lindeløv, A. Brask, S.K. Andersen, Scaling up the spray drying process from pilot to production scale using an atomized droplet size criterion, Pharm. Res. 25 (2008) 1610-1620.

[11] E. Babinsky, P.E. Sojka, Modeling drop size distributions, Prog. Energy Combust. Sci. 28 (2002) 303-329.

[12] M. Liu, Y. Duan, T. Zhang, Y. Xu, Evaluation of unsteadiness in effervescent sprays by analysis of droplet arrival statistics – The influence of fluids properties and atomizer internal design, Exp. Therm. Fluid Sci. 35 (2011) 190-198.

[13] N. Kannadasan, K. Ramanathan, S. Suresh, Comparison of heat transfer and pressure drop in horizontal and vertical helically coiled heat exchanger with CuO/water based nano fluids, Exp. Therm. Fluid Sci. 42 (2012) 64-70.

[14] S. Suresh, K.P. Venkitaraj, P. Selvakumar, M. Chandrasekar, Effect of Al2O3–Cu/water hybrid nanofluid in heat transfer, Exp. Therm. Fluid Sci. 38 (2012) 54-60.

[15] S. Yao, J. Zhang, T. Fang, Effect of viscosities on structure and instability of sprays from a swirl atomizer, Exp. Therm. Fluid Sci. 39 (2012) 158-166.

[16] D. Walton, C. Mumford, Spray dried products-characterization of particle morphology, Chem. Eng. Res. Design. 77 (1999) 21-38.

[17] P. Meenan, K. Roberts, P. Knight, K. Yuregir, The influence of spray drying conditions on the particle properties of recrystallized burkeite (Na_2CO_3•$(Na_2SO_4)_2$), Powder Technol. 90 (1997) 125-130.

[18] A.A. Ambike, K. Mahadik, A. Paradkar, Spray-dried amorphous solid dispersions of simvastatin, a low T g drug: in vitro and in vivo evaluations, Pharm. Res. 22 (2005) 990-998.

[19] M.A. Mohamed, S.A. Halawy, Non-isothermal kinetic and thermodynamic study for the dehydration of copper(II) chloride dihydrate and nickel chloride hexahydrate, J. Therm. Anal. 41 (1994) 147-159.

[20] O.G. Polyachenok, E.N. Dudkina, L.D. Polyachenok, Thermal stability and thermodynamics of copper (II) chloride dihydrate, J. Chem. Thermodyn. 41 (2009) 74-79.

[21] O.G. Polyachenok, E.N. Dudkina, N.V. Branovitskaya, L.D. Polyachenok, Formation of super disperse phase and its influence on equilibrium and thermodynamics of thermal dehydration, Thermochimica. Acta. 467 (2007) 44-53.

[22] N. Busscher, J. Kahl, P. Doesburg, G. Mergardt, A. Ploeger, Evaporation influences on the crystallization of an aqueous dihydrate cupric chloride solution with additives, J. Colloid Interface Sci. 344 (2010) 556-562.

[23] T. Keskitalo, J. Tanskanen, T. Kuokkanen, Analysis of key patents of the regeneration of acidic cupric chloride etchant waste and tin stripping waste, Resour. Conserv. Recycling. 49 (2007) 217-243.

[24] M. Mezhericher, A. Levy, I. Borde, Theoretical drying model of single droplets containing insoluble or dissolved solids, Drying Technol. 25 (2007) 1025-1032.

[25] G.D. Marin, G.F. Naterer, K. Gabriel, Evaporative drying of cupric chloride droplets in a thermochemical cycle of hydrogen production, Univ. of Ontario Inst. of Tech., Oshawa, MASc Thesis 2008.

[26] K.C. Patel, X.D. Chen, Surface-center temperature differences within milk droplets during convective drying and drying-based Biot number analysis, AICHE J. 54 (2008) 3273-3290.

[27] K.C. Patel, X.D. Chen, Prediction of spray-dried product quality using two simple drying kinetics models, J. Food Process Eng. 28 (2005) 567-594.

[28] I.K. Puri, Environmental Implications of Combustion Processes, CRC Press, Boca Raton, Florida, 1993.

[29] P. Bahadorani, University of Ontario Institute of Technology, Evaporative Heat and Mass Transfer with Solubility Driven Solidification of Aqueous Droplet Flows, Univ. of Ontario Inst. of Tech., Oshawa, MASc Thesis 2009.

[30] W. Ranz, W. Marshall, Evaporation from drops, Chem. Eng. Prog. 48 (1952) 141-146.

[31] T.W. Hoffman, L.L. Ross, Theoretical investigation of the effect of mass transfer on heat transfer to an evaporating droplet, Int. J. Heat Mass Transfer. 15 (1972) 599-617.

[32] R. Clift, J.R. Grace, M.E. Weber, Bubbles, Drops, and Particles, Dover Publications, Mineola, New York, 2005.

[33] S.S. Sazhin, Advanced models of fuel droplet heating and evaporation, Prog. Energy Combust. Sci. 32 (2006) 162-214.

[34] M. Slowikowski, Evaporative drying of cupric-chloride droplets in a thermo-chemical cycle of hydrogen production, Univ. of Ontario Inst. of Tech., Oshawa, MASc Thesis 2012.

[35] R.W. Tate, J. Marshall W.R., Atomization by centrifugal pressure nozzles, Chem. Eng. Prog. 49 (1953) 4-5.

[36] P. Rosin, E. Rammler, The laws governing the fitness of powdered coal, J. Inst. Fuel. 7 (1953) 29-33.

[37] A.S. Mujumdar, Handbook of Industrial Drying, CRC, Boca Raton, Florida, 2006.

[38]] X.D. Chen, S.X.Q. Lin, Air drying of milk droplet under constant and time-dependent conditions, AICHE J. 51 (2005) 1790-1799.

Table1: Steps in the Copper-Chlorine Cycle [**11**]

Step	**Reaction**	**Temp. Range (°C)**	**Feed Output***	
1	$2CuCl(aq) + 2HCl(aq) \rightarrow H_2(g) + 2CuCl_2(aq)$	<100 (electrolysis)	Feed: Output:	Aqueous CuCl and HCl + V + Q H_2 + $CuCl_2$ (aq)
2	$CuCl_2(aq) \rightarrow CuCl_2(s)$	<100	Feed: Output:	Slurry containing HCl and $CuCl_2$ + Q Granular $CuCl_2$ + H_2O/HCl vapours
3	$2CuCl_2(s) + H_2O(g) \rightarrow Cu_2OCl_2(s) + 2HCl(g)$	400	Feed: Output:	Powder/granular $CuCl_2$ + $H_2O(g)$ + Q Powder/granular Cu_2OCl_2 + 2HCl (g)
4	$Cu_2OCl_2(s) \rightarrow 2CuCl(l) + 1/2O_2(g)$	500	Feed: Output:	Powder/granular $Cu_2OCl_2(s)$ + Q Molten CuCl salt + oxygen
* Q = thermal energy, V = electrical energy				

Table 2: Particle size definitions

Name	**Denotation**	**Value**
Number mean diameter	d_{10}	$\sum d\ /N_p$
Surface mean diameter	d_{20}	$\sqrt{\sum d^2\ /N_p}$
Volume mean diameter	d_{30}	$\sqrt[3]{\sum d^3\ /N_p}$
Sauter mean diameter	d_{32}	$\sum d^3 / \sum d^2 = {d_{30}}^3 / {d_{20}}^2$

Table 3: Experiments performed with their respective varied parameters

Trial no.	**Ambient air**		**Hot air**			**Atomization air**		**Atomization liquid**	
	Room Temp. C	Relative Humidity %	Inlet Temp. C	Outlet Temp. C	Flow rate m^3/min	Flow rate m^3/hr	Pressure bar	Flow rate lit/hr	Temp. C
1	22	23	60	35	1	3	4	0.5	22
2	23	26	80	40	1	2.9	4	0.5	23
3	24	23	120	58	1	3.1	4	0.5	24
4	23.5	24	160	70	1	3.1	4	0.5	23.5
18	22.5	23	200	30	1	5.8	2.5	0.5	22.5
30	22.5	23	200	72	1	5.2	2.5	0.5	22.5
31	22.5	23	120	60	1	5.1	2.5	0.5	22.5
33	21.5	23	80	40	0.8	4	4	0.5	21.5
36	21.5	23	200	80	1	2.95	2	0.5	21.5

Table 4: Parameter values for curve fits

	Temp.	**log normal**		**upper limit**			**root normal**		**Rosin-Rammler**	
Run no.	^{o}C	sigma	*d*	*d*	*d*	d_{max}	sigma	*d*	q	d
1	60C	1.49	17	1.63	20.2	103.8	0.83	16.4	2.78	18.6
2	80C	1.33	15.5	1.39	18	123.7	0.45	15	4.13	16.4
3	120C	1.45	5.9	1.5	6.4	78.4	0.45	5.8	3.06	6.5
4	160C	1.52	6.4	1.56	6.8	97	0.51	6.2	2.73	7
27	120C	2.00	12.2	1.9	13.1	100	1.1	12.2	1.83	15.1
33	160C	2.08	21.2	2.35	26	100	1.35	20.1	1.83	24.7
36	200C	2.01	6.5	2.07	6.9	100	0.74	6.1	1.9	7.5

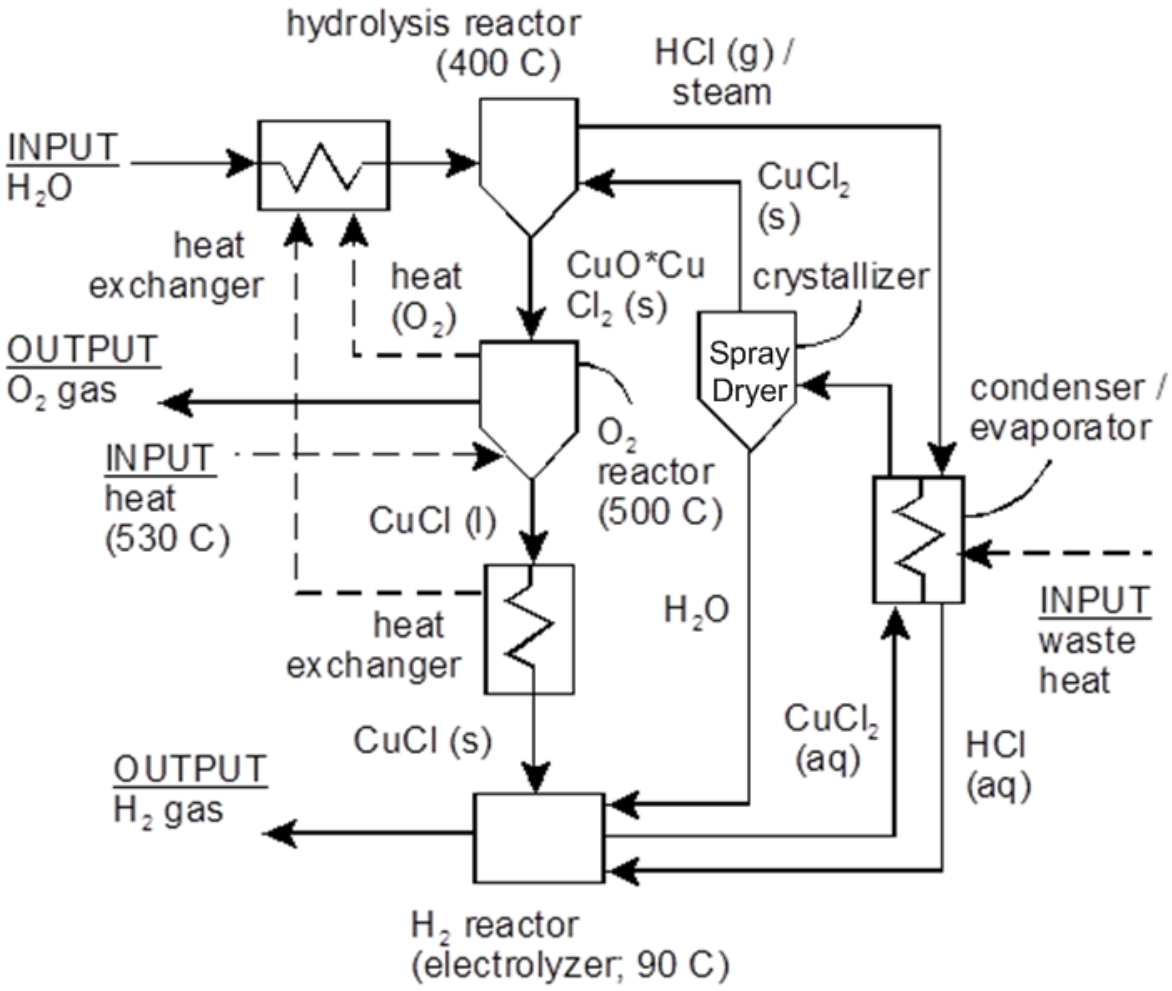

Fig. 1: Schematic of the Copper-Chlorine Cycle [4]

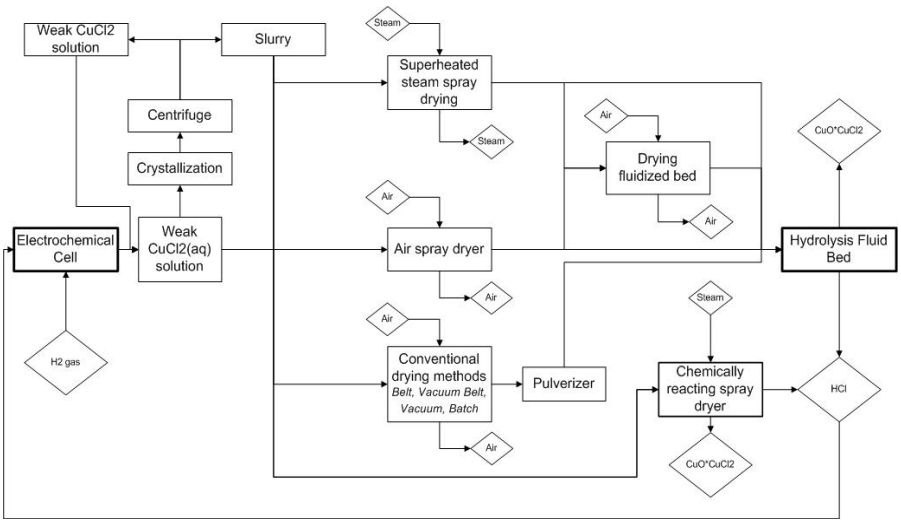

Fig. 2: Summary of DCC processing options for the Cu–Cl cycle

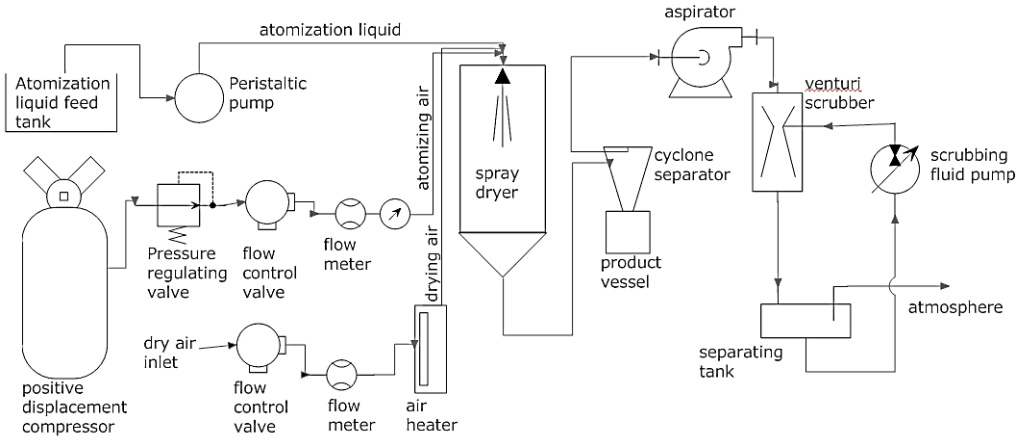

Fig. 3: Schematic of spray drying apparatus

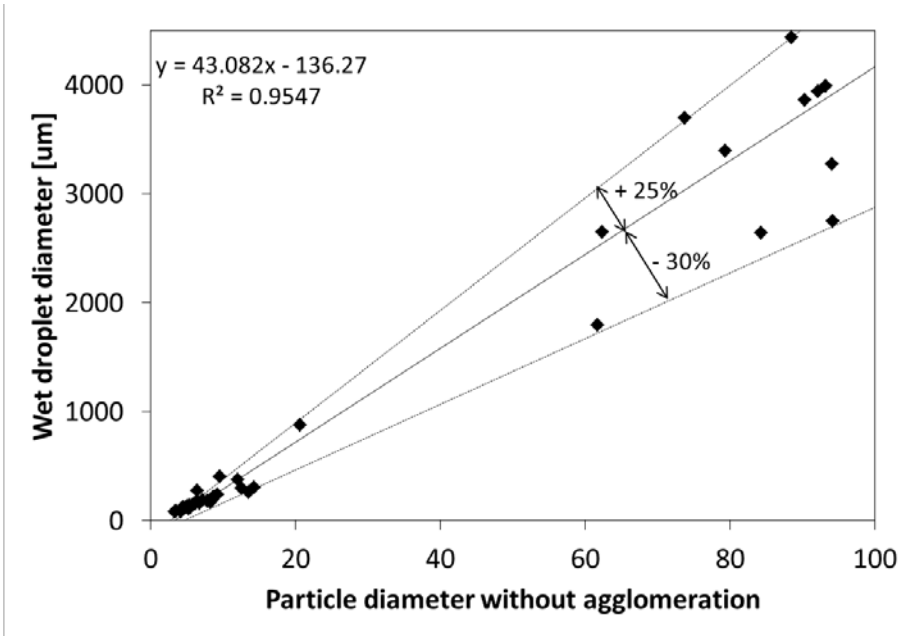

Fig. 4: Discounting droplet drying, with non-spherical particles

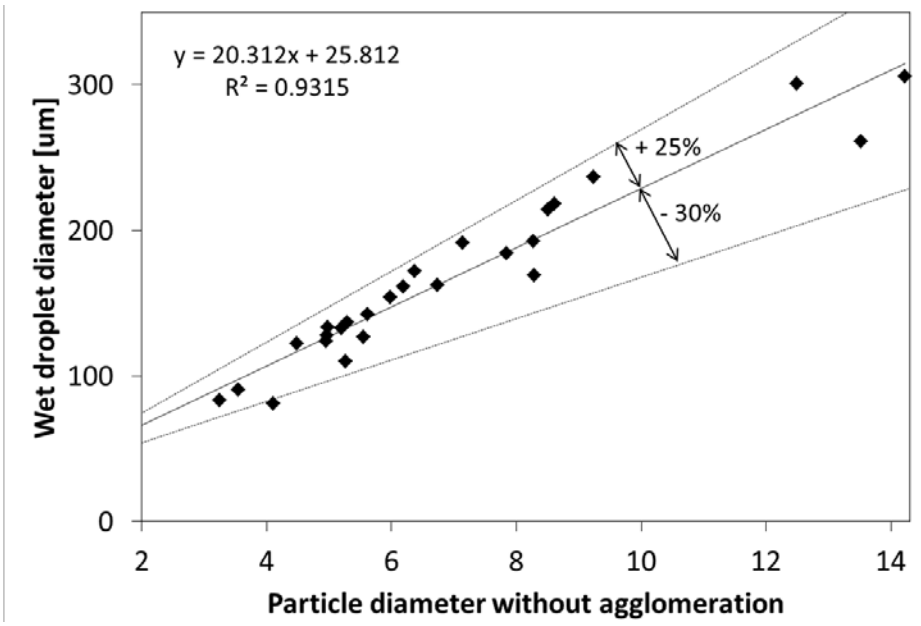

Fig.5: Discounting droplet drying, without non-spherical particles

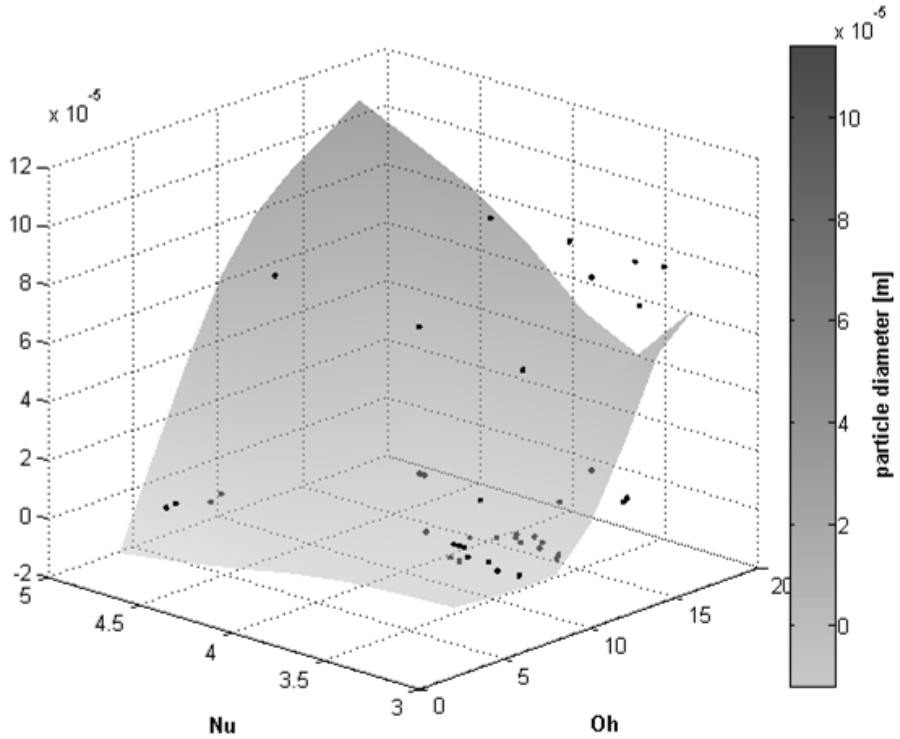

Fig. 6: Particle diameter vs. Ohnesorge and Nusselt numbers

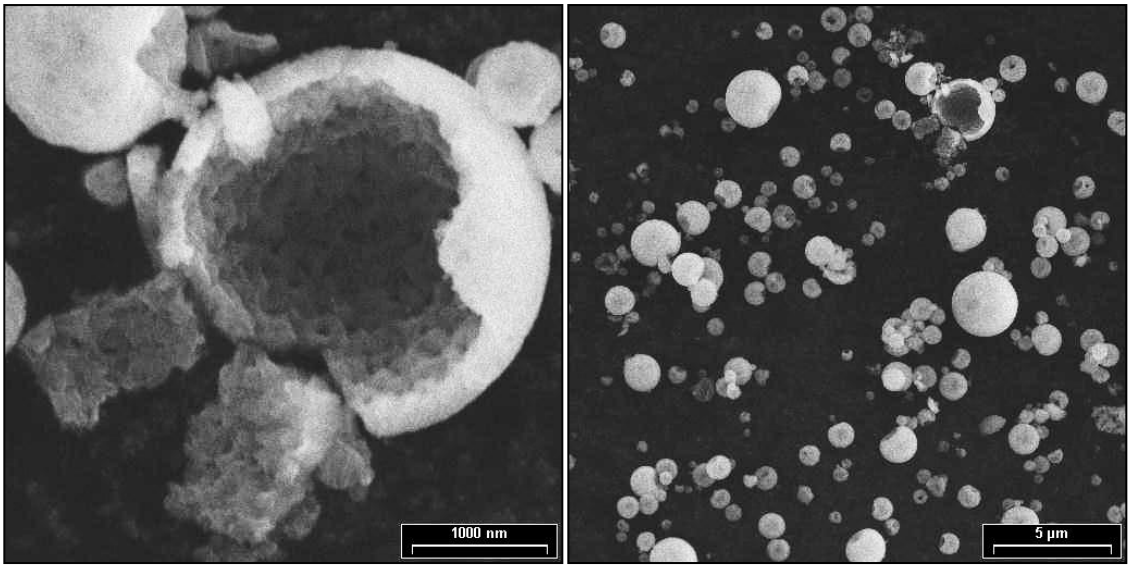

Fig. 7: Particles dried at 120^{o}C

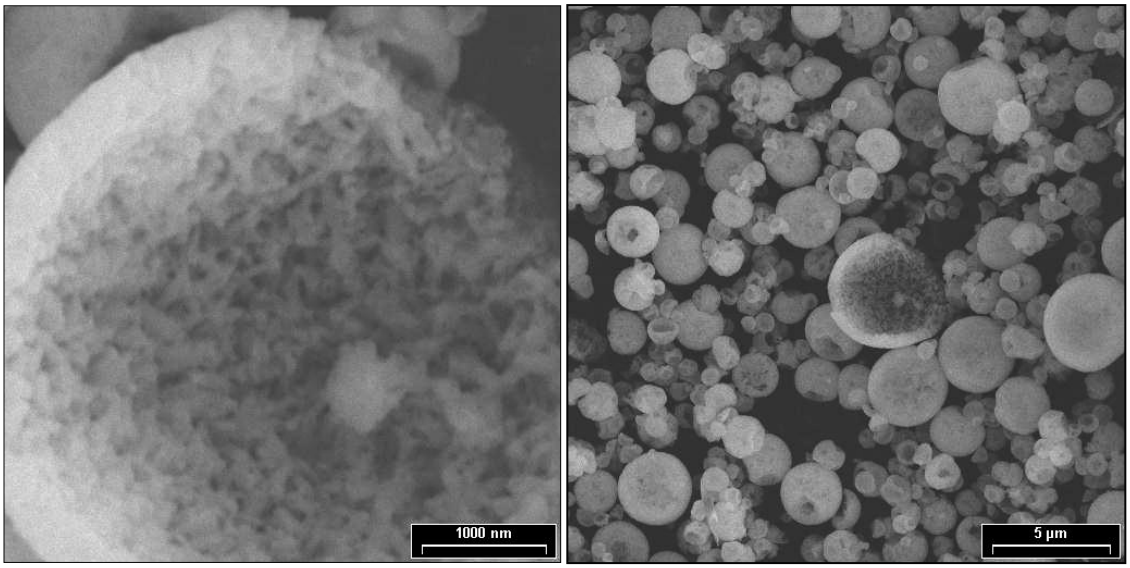

Fig.8: Particles dried at 200^{o}C

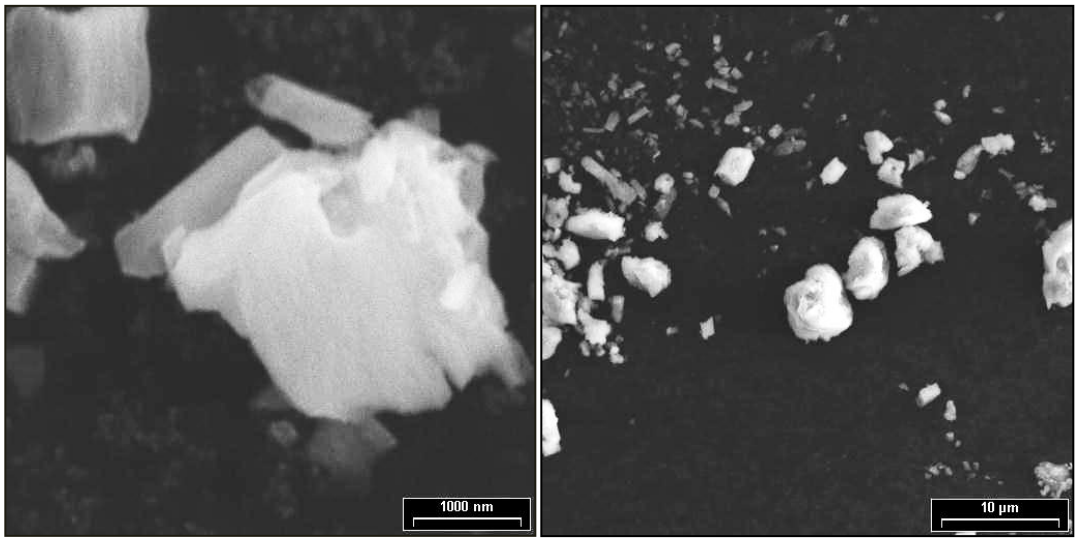

Figure 0.9: Particles dried at 60^{o}C

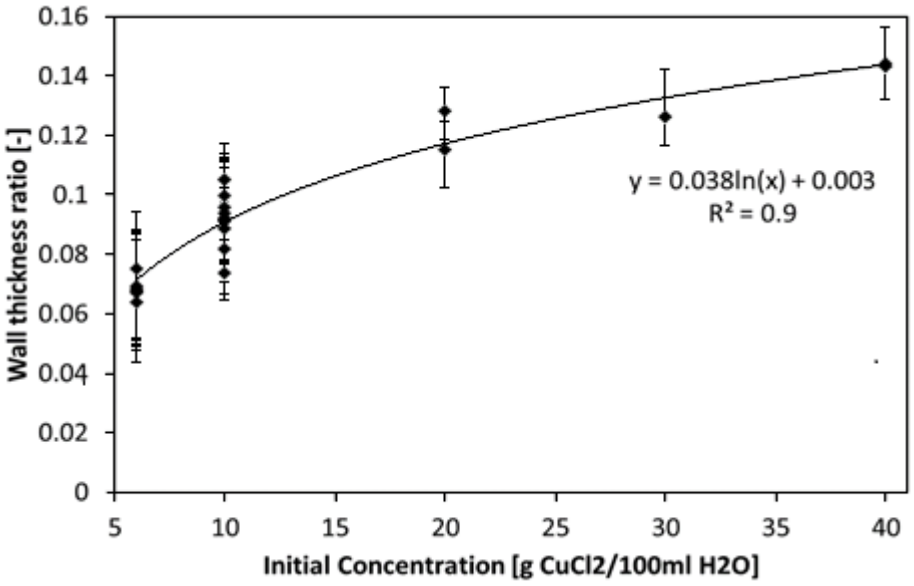

Fig. 10: Initial concentration vs. wall thickness ratio

- Summary -		- Percentiles -		- Peaks Summary -		
Data	Value	%Tile	Size(um)	Dia(um)	Vol%	Width
MV(um):	90.48	10.00	1.899	229.5	37.7	64.69
MN(um):	1.568	20.00	2.353	5.77	23.9	8.23
MA(um):	4.45	30.00	3.13	3.37	12.0	0.76
CS:	1.347	40.00	4.08	2.062	26.4	1.17
SD:	116.6	50.00	5.68			
		60.00	18.97			
Mz:	81.07	70.00	205.1	UDefName		UDefData
σι:	98.98	80.00	227.1			
Ski:	0.969	90.00	249.8			
Kg:	0.513	95.00	269.9			

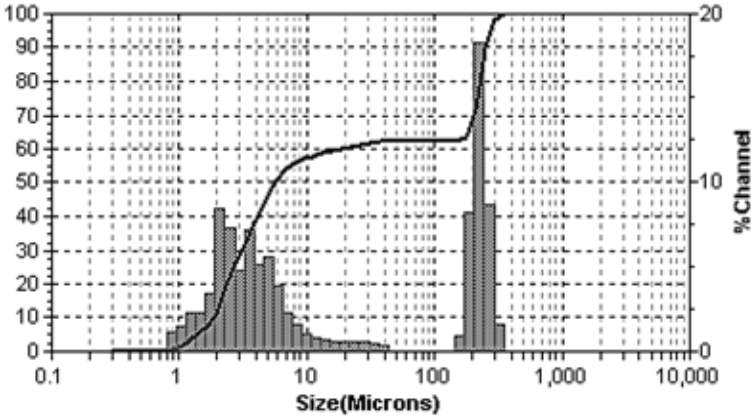

Fig. 11: Results from laser diffractometer case no. #39-2

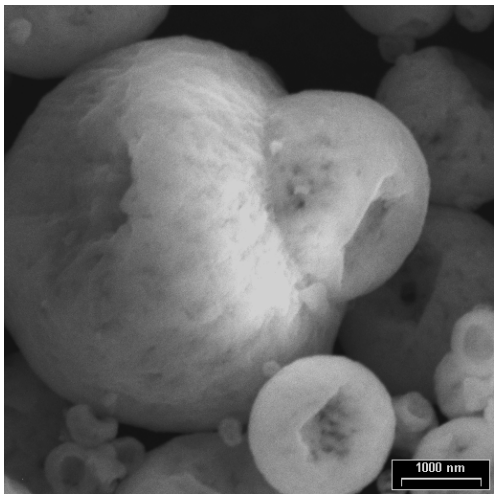

Fig. 12: Run 21 droplet coalescence during mass transfer and drying

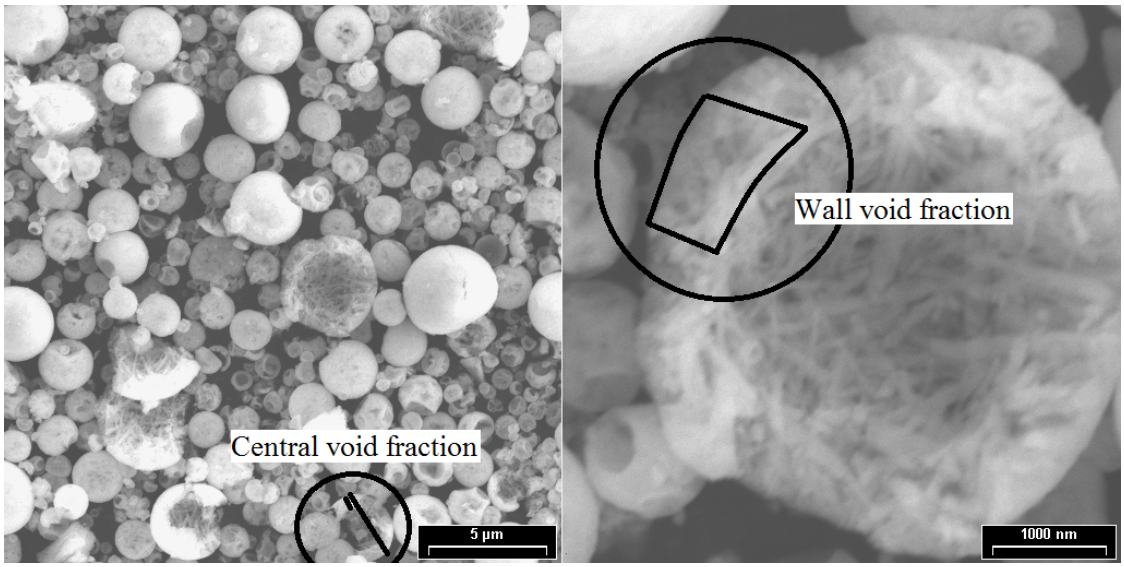

Fig. 13: Central void fraction and wall void fraction

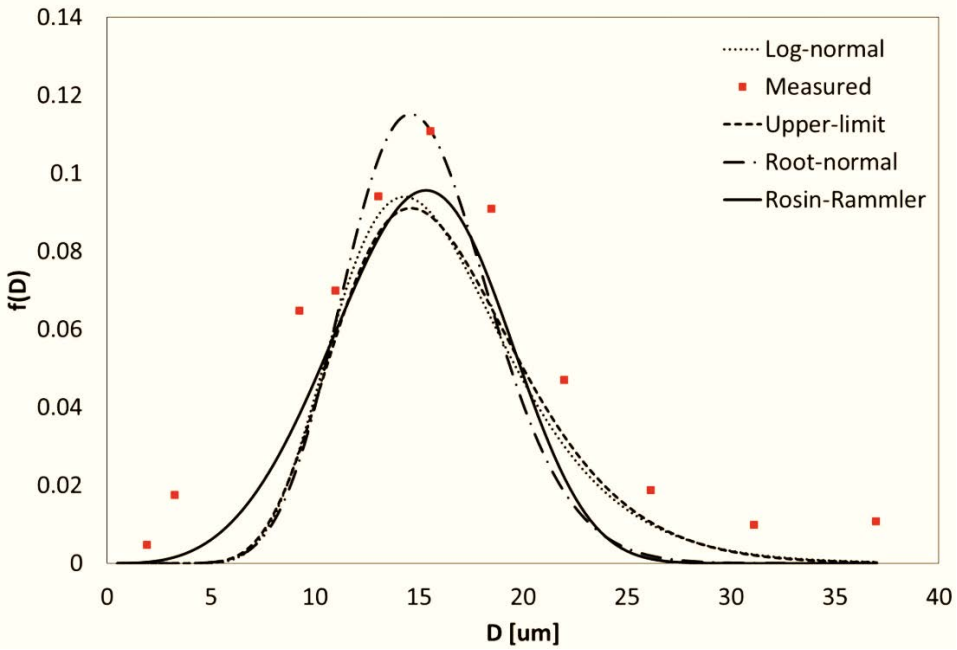

Fig. 14: Case no. 2 (80°C, 0.7mm nozzle) particle results

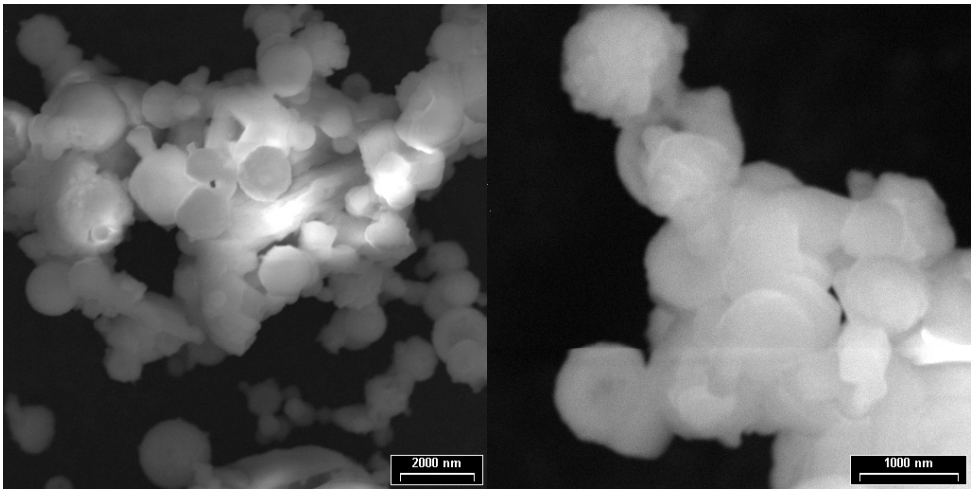

Fig. 15: Case no. 2 (80°C, 0.7mm nozzle) SEM results

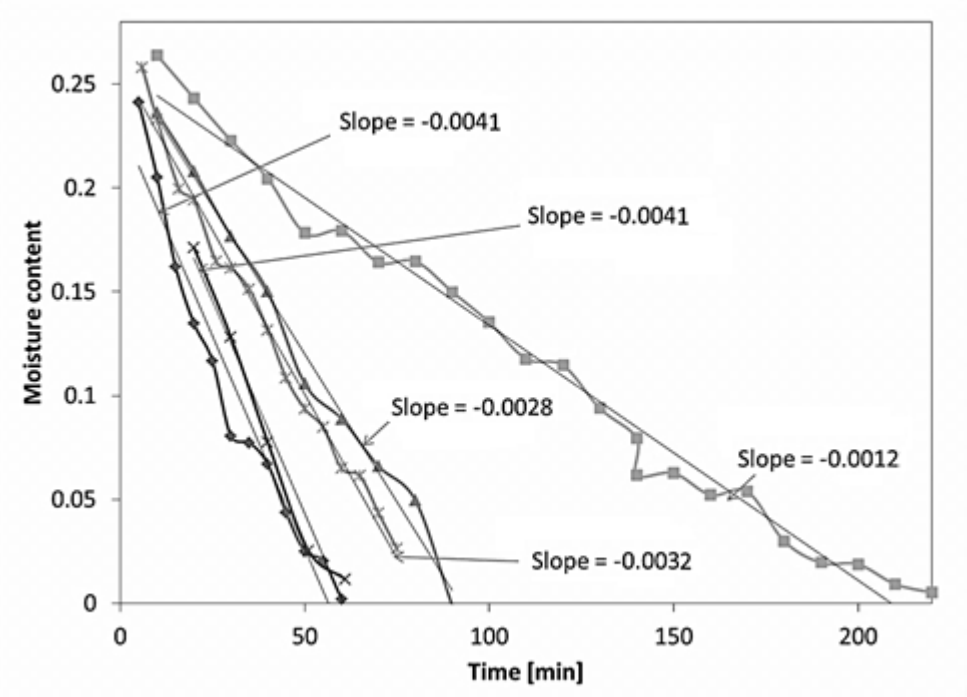

Fig. 16: Convective drying rate experiments

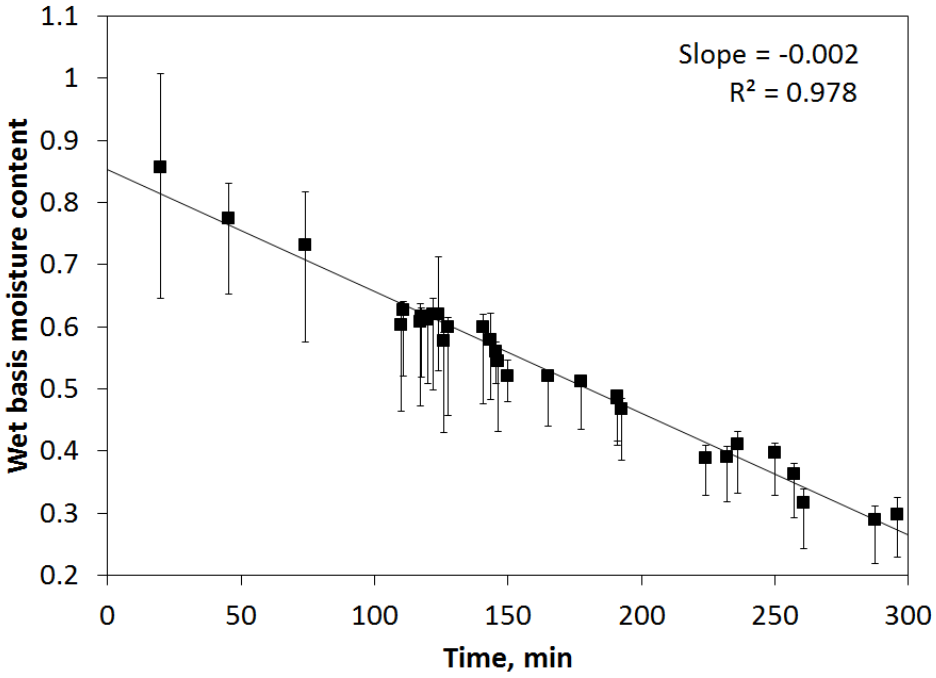

Fig. 17: Drying rate determined from slurry data at 100°C